

# RSC Advances



This is an *Accepted Manuscript*, which has been through the Royal Society of Chemistry peer review process and has been accepted for publication.

*Accepted Manuscripts* are published online shortly after acceptance, before technical editing, formatting and proof reading. Using this free service, authors can make their results available to the community, in citable form, before we publish the edited article. This *Accepted Manuscript* will be replaced by the edited, formatted and paginated article as soon as this is available.

You can find more information about *Accepted Manuscripts* in the [Information for Authors](#).

Please note that technical editing may introduce minor changes to the text and/or graphics, which may alter content. The journal's standard [Terms & Conditions](#) and the [Ethical guidelines](#) still apply. In no event shall the Royal Society of Chemistry be held responsible for any errors or omissions in this *Accepted Manuscript* or any consequences arising from the use of any information it contains.

# Reductant-Assisted Synthesis, Characterization and Photovoltaic Characteristics of Ligand-Protected Gold Nanoparticles

Naveed Shahzad<sup>a</sup>, Fuyi Chen<sup>a,\*</sup>

<sup>a</sup> State Key Laboratory of Solidification Processing, Northwestern Polytechnical University, Xian 710072, China

\* Corresponding author.

Prof. Fuyi Chen; E-mail ID: fuyichen@nwpu.edu.cn

Tel./fax: +86 029-88492052.

State Key Laboratory of Solidification Processing, Northwestern Polytechnical University, Xian 710072, China

## Abstract

Metal clusters (CLs) and nanoparticles (NPs) are promising on account of their unique properties which cannot be achieved from their bulk counterparts. Discrete electronic excitations in metal CLs and the characteristic surface plasmon resonance (SPR) phenomenon in metal NPs make them optically attractive and versatile photosensitizers in photovoltaic (PV) applications. Visible-light driven photo-electrochemical (PCE) response of plasmonic sensitizer in metal NPs/semiconductor composite assembly can be tuned with plasmonic metal NPs sizes. Therefore, it is highly desirable to explore PEC response of a plasmonic sensitizer as a function of its NPs sizes. In this work, the study focusing on the PEC performance of plasmonic sensitizer as a function of its NPs sizes has

been realized through synthesizing a series of ligand-protected Au NPs at ambient conditions using varied reductants, since each reductant in coordination with ligand forms metal ion complexes which influence the reduction potentials of metals through variation in the pH of the system, and ultimately, these changes affect the reaction dynamics and tune the NPs sizes and morphology. Superior PEC response of glucose-assisted synthesis of Au NPs in NPs sensitized solar cells (NPSCs) with power conversion efficiency greater than 1.5 % has been observed, and attributed to the relatively finer NPs sizes and uniform distribution on TiO<sub>2</sub> photoanodes. It is expected that our study assists in exploration of different sized Au NPs in diverse applications.

**Key words:** Ligand-protected metal NPs; plasmonic sensitizers; photo-electrochemical behavior; surface plasmon resonance; electrochemical impedance spectroscopy

## 1. Introduction

Dye sensitized solar cells (DSSCs) have been intensively studied worldwide, since its inception in 1991 when a group of renowned researchers laid the foundations of an efficient and low cost DSSC.<sup>1</sup> In DSSCs, the sensitizer is one of the main components; which owing to its enhanced light absorption capability provides photo-excited electrons through interaction with light. Organic dyes, metal complexes, and perovskite compounds<sup>2, 3</sup> have widely been employed as sensitizers in DSSCs. Some dyes are expensive (Ruthenium based complexes), while the other ones may pose environmental concerns (Lead based complexes). These issues call for an alternative sensitizer to be explored. In recent years, metal CLs capped by stabilizing ligand are becoming fascinating materials because of their unique properties considered to be intermediate between molecular species and bulk NPs.<sup>4</sup> Stabilizing shells or ligands such as such as thiolates<sup>4, 5</sup> provide stability and protection to metal CLs against oxidization, and provide a delicate control on particle sizes. PEC analysis of plasmonic metal CLs<sup>6</sup>, their optical absorption spectra<sup>7</sup>, and their photovoltaic

properties have extensively been explored.<sup>8</sup> Charge transfer mechanism and power conversion efficiency (PCE) of ligand-protected metal CLs greater than 2 % have recently been reported in the literature.<sup>5</sup> Apart from monometallic metal CLs, it has been demonstrated, in our previous report, that bimetallic CLs also are a unique class of photosensitizers.<sup>9</sup> In addition to metal CLs, plasmonic metal NPs (especially Au NPs) are also regarded as promising and attractive optical materials owing to the unique phenomenon such as surface plasmon resonance<sup>10, 11</sup> and surface enhanced Raman scattering.<sup>12</sup>

NPs have a wide-range of optical, electronic, catalytic, optoelectronic applications etc., where one of the important factors that can potentially influence their properties is their size and morphology.<sup>10, 13</sup> More specifically, SPR characteristics,<sup>14</sup> extinction coefficient,<sup>15</sup> and photocatalytic properties<sup>16</sup> are size-dependent for Au NPs, and therefore, call for the exploration of PCE response as a function of Au NPs sizes, since the visible-light driven PEC performance of plasmonic sensitizers as a function of their NPs sizes in metal NPs/semiconductor composite assembly still remains a challenge. Moreover, in Au NPs/ TiO<sub>2</sub> composite assembly, the size of Au NPs also influences the shift in equilibrium Fermi level, and thus modifies the photoinduced charge transfer efficiency in Au NPs/TiO<sub>2</sub> composite assembly.<sup>17</sup> Therefore, it is highly desirable to explore the PEC performance of Au NPs sensitized solar cells, as a function of NPs sizes. For stabilization of Au NPs, we have used L-glutathione ligand, since Au NPs not protected with stabilizing ligand may cause photo-corrosion, which limits the PEC performance.<sup>11</sup> For the synthesis of different sized glutathione Au NPs (Au-GSH NPs), a widely-used metal salt reduction method has been employed on account of its simplicity, versatility and low cost. In this method, the change in synthetic conditions, such as temperature, initial concentration of reductant, and metal salt might be one effective approach to tune the sizes of Au-GSH NPs, since the complex

coordination mechanisms involved in metal precursors, ligands and reducing agents provide a structural control on the nanoparticle morphology.<sup>18, 19</sup> However, in this work, the synthesis of different-sized Au-GSH NPs has been realized through the use of varied reductants at ambient conditions, leading to manifestation of their imperative role as plasmonic sensitizer in NPSCs. Nucleation and growth of Au NPs are effected by the concentration of metal ions controlled by reductants, since each reductant in coordination with ligand forms metal ion complexes which influence the reduction potentials of metals through variation in the pH of the system, and ultimately, these changes affect the reaction dynamics and tune the NPs sizes and morphology.<sup>18, 19</sup> Widely-available reductants such as sodium borohydrite,<sup>6</sup> citrates<sup>18</sup>, glucose<sup>20</sup> etc. are employed for the synthesis of metal NPs. A series of Au-GSH NPs has been synthesized at ambient conditions using reductants such as sodium borohydrite, glucose and tri-sodium citrate to reduce  $\text{AuCl}_3 \cdot \text{HCl} \cdot 4\text{H}_2\text{O}$  (gold metal precursor), and demonstrated their influence on formed Au NPs sizes followed by manifestation of functional performance of the resultant different sized Au-GSH NPs as plasmonic sensitizer in NPSCs in conjunction with mesoporous  $\text{TiO}_2$  semiconductor. For convenience, Au-GSH NPs synthesized using reductants glucose, sodium borohydrate, and tri-sodium citrate have been arbitrary marked as Au-GSH-B, Au-GSH-C and Au-GSH-D NPs, respectively. We also have synthesized, for comparison, Au-GSH NPs without using external reductant, and the synthesized NPs are identified as Au-GSH-A NPs. During investigation, it has been found that Au-GSH-B NPs synthesized using glucose, exhibit superior PEC response. Furthermore, optical absorption spectroscopy, electron microscopy, electrochemical impedance spectroscopy (EIS), open circuit voltage ( $V_{oc}$ ) decay method and Mott-Schottky (M-S) analysis have been conducted to elucidate the processes occurring inside NPSCs. We expect that our work on synthesis of different sized Au-GSH NPs by reductant-assisted synthesis, will contribute

significantly to synthesis chemistry rendering these different sized Au-GSH NPs amenable to further exploration in a diverse range of applications, with particular examples being their exploration coupled with suitable dyes in photovoltaic cells<sup>21</sup>, synergistic effects of Au NPs and CLs to enhance the optical activity in energy applications<sup>22, 23</sup>, size-dependent extinction coefficient of Au NPs,<sup>15</sup> and tuning the photodynamic therapy and activity through different sized Au NPs in medical applications<sup>24</sup>.

## 2. EXPERIMENTAL SECTION

All reagents were used as analytical grades without any further purification. We synthesize mesoporous TiO<sub>2</sub> (mTiO<sub>2</sub>), glutathione-protected Au NPs, Pt counter electrode, and fabricate NPs sensitized solar cells.

### 2.1 Synthesis of TiO<sub>2</sub> Colloidal Solution and ligand protected gold NPs

Mesoporous TiO<sub>2</sub> has been synthesized according to the method published in the literature.<sup>25</sup> We employ sol-hydrothermal synthesis for TiO<sub>2</sub> colloidal solution. The details of the synthesis of mTiO<sub>2</sub> have been mentioned in the supporting information. Au-GSH-A NPs have been synthesized according to the literature with a little modification<sup>26</sup> and Au-GSH-B, Au-GSH-C and Au-GSH-D NPs by following the procedure mentioned in the literature with some modification in the use of reductants.<sup>6</sup> Supporting information can be viewed for gold NPs synthesis.

### 2.2 Fabrication of NPSCs

To explore the photo-electrochemical performance of these ligand-protected gold NPs synthesized at ambient conditions using different reductants, we follow the procedure reported in the literature<sup>5</sup> to fabricate NPSCs. Mesoporous TiO<sub>2</sub> spin-coated on FTO and modified with Au-GSH NPs has

been used as photoanode and Pt coated FTO as counter electrode in the presence of cobalt-based redox shuttle. Schematically the structure of NPs sensitized solar cells have been shown in the Figure 1.

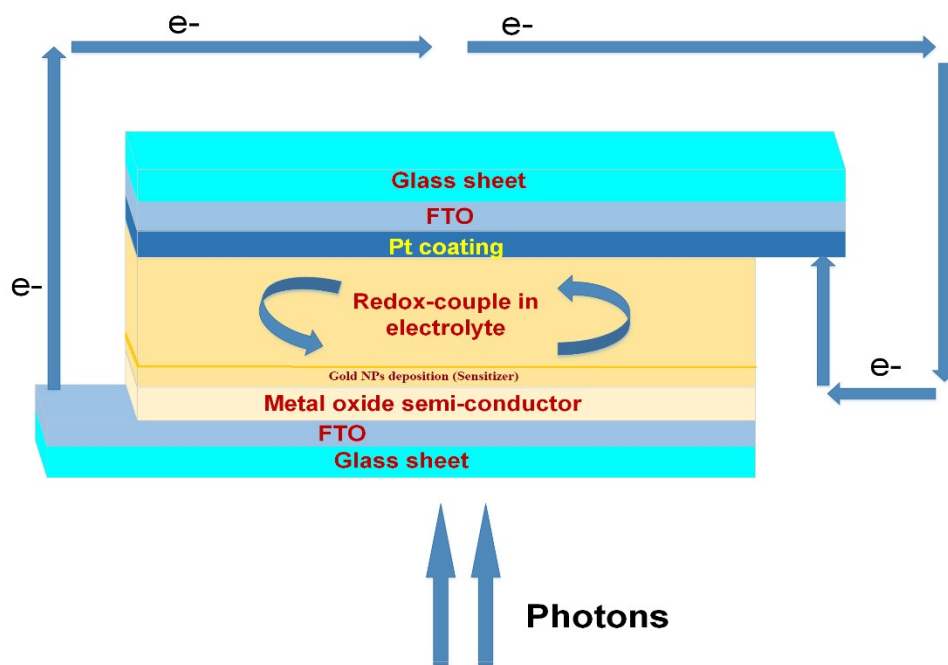


Figure 1. Schematic representation of NPSCs

Fabrication of  $\text{TiO}_2$  photoanodes, Pt counter electrode and assembly of NPSCs has been described, in details, in the Supporting information.

### 2.3 Characterization

The  $\text{TiO}_2$  photoanodes were characterized by SEM (JSM, 6390A) with energy dispersive X-ray spectroscopy (SEM-EDS) for surface morphology. X-ray diffraction (XRD) technique was employed to determine the crystallite size of  $\text{TiO}_2$  and its crystal phase. The XRD data were obtained in the  $2\theta$  range between  $20$  and  $70^\circ$  using an Xpert-PRO diffractometer. HRTEM and selected area electron diffraction (SAED) (TECNAI instrument) were conducted to characterize

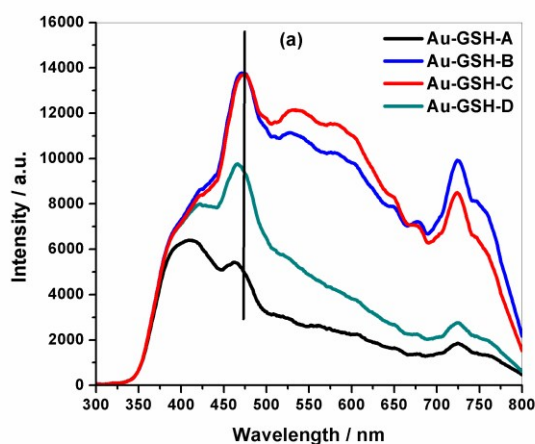
the CLs. Optical absorption spectra were obtained using Zolix Omni- $\lambda$  300 Monochromator/Spectrograph and DCS103 Data Acquisition System. All PEC measurements were conducted under visible light generated through 300 W Xenon lamp with 90 mW/cm<sup>2</sup> incident power using CHI660C electrochemical workstation. EIS,  $V_{oc}$  decay method and M-S analysis were performed on assembled devices using Co (II) / Co (III) redox couple on CHI660C electrochemical workstation. Active area of each device was marked as 0.145cm<sup>2</sup>. EIS was performed under dark by at  $V_{oc}$  using 10mV amplitude and frequency in the range of 1Hz to 100 KHz. The resultant spectra were fitted by using ZView software. M-S plots were obtained at amplitude of 10mV with voltage in the range of +1 to -1 V.

### 3. Results and discussion

#### 3.1 Optical absorption spectroscopy of Au-GSH NPs

Plasmonic metals such as Au, Ag, Cu etc. usually possess a sharp absorption peaks which are due to their localized surface plasmon resonance (LSPR) phenomenon arising from the collective oscillations of free electrons in response to an incident light.<sup>27</sup> Optical absorption spectra of dispersions of Au-GSH-A, Au-GSH-B, Au-GSH-C and Au-GSH-D NPs have been presented in Figure 2. Intensity of absorption signals are shown in Figure 2 (a), where the maximum intensity of absorption signals of Au-GSH-B and Au-GSH-C NPs is observed to be red-shifted in comparison with that of Au-GSH-A NPs and Au-GSH-D NPs indicating a wide range of optical absorption. These absorption signals are based on only visible range of solar spectrum. Different NPs exhibit different absorption signal intensity indicating a varied response to visible light. Maximum intensity of absorption signals is found to be at 410 nm, 465 nm, 470 nm and 455 nm for Au-GSH-A, Au-GSH-B, Au-GSH-C and Au-GSH-D NPs, respectively. Before the wavelength

of 400 nm; all four types of Au-GSH NPs exhibit almost similar absorption trend, however, beyond 400 nm the absorption is distinctly different from one another suggesting a wide absorption band extending towards visible region having longer wavelengths. Figure 2 (b) shows the optical absorption spectra where Au-GSH-C NPs exhibit a wide absorption band between the wavelengths of 450 nm to 700 nm owing to the LSPR effect of Au NPs. The SPR peak of Au-GSH-C NPs is not very sharp since the NPs sizes are very small. The SPR peak of Au NPs shifts towards longer wavelengths with an increase in particle size. In Au-GSH-C NPs, the LSPR peak is centered at 550 nm, slightly red-shifted than that observed in Au NPs and gold nanowires reported in the literature.<sup>28</sup> Such wide SPR absorption band between the wavelengths of 450 nm to 700 nm has not been observed in Au-GSH-A, Au-GSH-B and Au-GSH-D NPs. Moreover, optical absorbance is influenced by the NPs size and particle volume. Different sizes of metal NPs exhibit varied absorption bands in optical absorption spectra. As the NPs size increases, their band gaps become smaller and corresponding absorption spectra extends towards longer wavelength.<sup>29</sup>



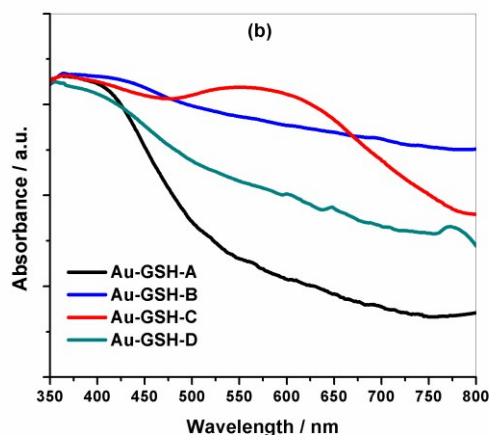


**Figure 2.** Optical absorption spectra of Au-GSH NPs dispersed in DI water, (a) Intensity of optical absorption signals, (b) optical absorbance spectra

### 3.2 Au-GSH NPs sizes and morphology

Transmission electron microscopy has been conducted on Au-GSH-A, Au-GSH-B, Au-GSH-C and Au-GSH-D NPs for the characterization of NPs morphology. TEM images are shown in the Figures 3. TEM image of Au-GSH-A NPs (Figure 3a) synthesized without any reductant has not been resolved appreciably which might be due to incomplete formation of Au NPs, since we synthesize all types of NPs at room temperature. Au-GSH-B NPs (Figure 3b) employing glucose reductant have core size in the range of 3~4 nm, whereas, Au-GSH-C NPs (Figure 3c) exhibit the core size in the range of 4~6 nm. Au-GSH-D NPs (Figure 3d) exhibit relatively larger NPs size likely due to agglomeration of individual NPs synthesized using tri-sodium citrate. Histograms showing the approximate distribution of NPs sizes have been shown in the Figure S1. High-resolution TEM has been performed for typically Au-GSH-C NPs to determine interfringe distances. In HRTEM image (Figure 3e), the interfringe distances of Au-GSH-C NPs have been measured to be around 0.24 nm, indicating the (111) plane spacing for FCC gold. These interfringe

distances are similar to Au-GSH-B and Au-GSH-D NPs, however, the HR-TEM could not resolve interfringe distances for Au-GSH-A NPs. Selected area electron diffraction (SAED) patterns have been obtained for Au-GSH-B and Au-GSH-C NPs, and are displayed as inset in the corresponding TEM images, which suggest the polycrystalline nature of Au-GSH NPs. Au-GSH-A NPs show lack of clear lines of demarcation between the individual NPs, which provide hurdles in the analysis of HR-TEM. Furthermore, EDX analysis of relatively finer NPs i.e. Au-GSH-B NPs has been performed and presented in Figure 3 (f) which indicates the presence of gold. The presence of Ni in EDX pattern shows the peaks of Ni substrate used for TEM analysis.

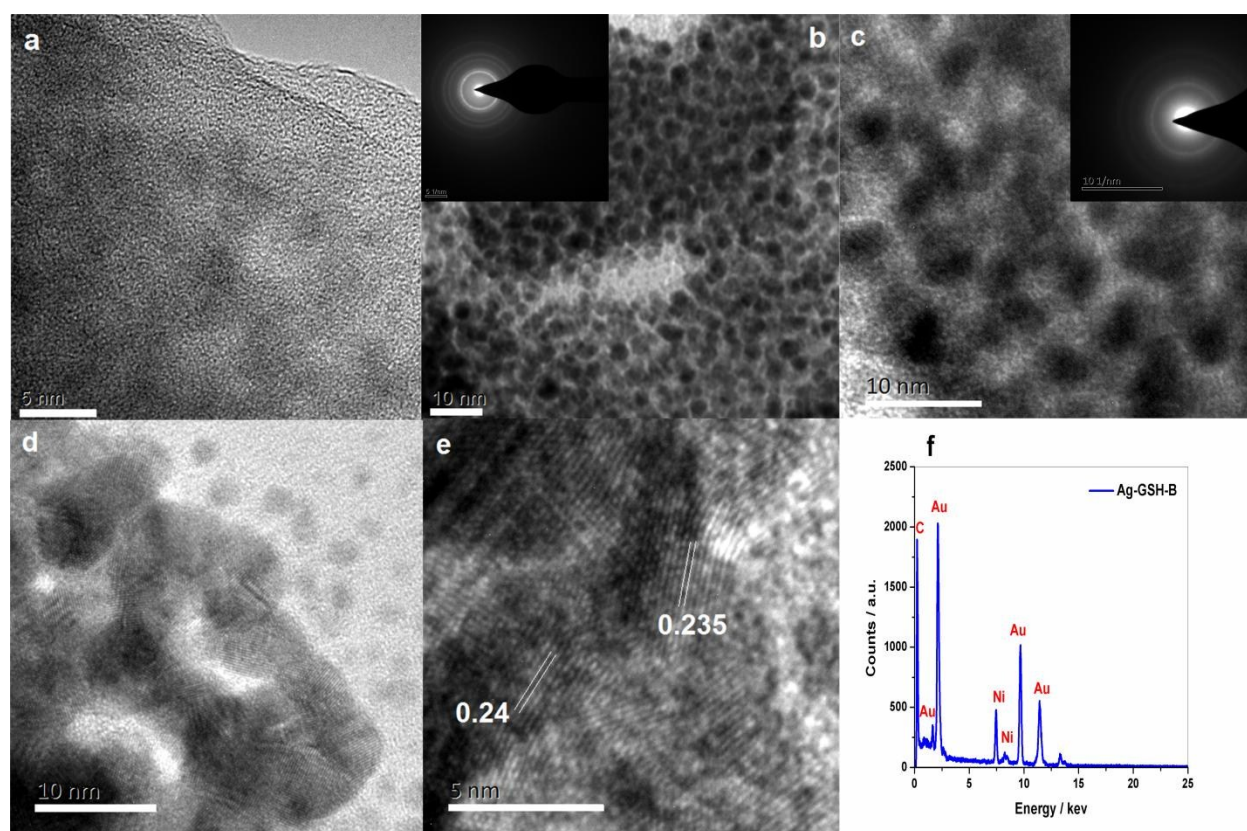


**Figure 3.** TEM images of (a) Au-GSH-A NPs, (b) Au-GSH-B NPs, (c) Au-GSH-C NPs, (d) Au-GSH-D NPs, (e) HR-TEM image of Au-GSH-C NPs, and (f) EDX analysis of Au-GSH-B NPs. SAED patterns of Au-GSH-B and Au-GSH-C NPs are shown as inset in the corresponding TEM images.

### 3.3 Morphology of mTiO<sub>2</sub> modified with Au-GSH NPs

TiO<sub>2</sub> semiconductor has been selected as a working electrode in NPSCs. Mesoporous morphology of TiO<sub>2</sub> has been obtained through controlled sintering process. XRD corroborates the presence of anatase phase of TiO<sub>2</sub> synthesized through sol-hydrothermal method. Anatase phase of TiO<sub>2</sub> and its mesoporous morphology are usually preferred in comparison with other phases and dense morphology.<sup>30</sup> XRD pattern of spin-coated mTiO<sub>2</sub> and its film thickness on FTO have been shown in Figure 4(a) and 4(b), respectively. Since XRD has been performed on TiO<sub>2</sub> coated FTO glass, therefore, FTO peaks are also present in Figure 3 (a). The anatase TiO<sub>2</sub> peaks are marked by the symbol (♦) in accordance with JCPDS # 21-1272, whereas the peaks marked by the symbol (Δ) are assigned to FTO substrate according to JCPDS # 46-1088. The crystallite size of mTiO<sub>2</sub> can be estimated from a famous Scherrer's equation:  $L = K\lambda / \beta \cos\Theta$ , where L is the crystallite size,  $\lambda$  is the wavelength of the X-ray radiation (CuK $\alpha$  radiations have been used with the wavelength of 0.1542nm), K is usually taken as 0.89, and  $\beta$  is the line width at half-maximum height (FWHM).<sup>31</sup> From Figure 4 (a), the crystallite size has been determined as 16.7 nm for spin-coated mTiO<sub>2</sub>. TiO<sub>2</sub> photoanodes were coated with Au-GSH NPs through immersion or soaking technique. XRD was performed on NPs-coated TiO<sub>2</sub> photoanodes to determine the peaks of Au NPs (not shown here). Au peaks have not been observed in XRD patterns of Au cluster-coated TiO<sub>2</sub>, which indicate a small amount of NPs that have been used to modify mTiO<sub>2</sub> and also the uniform distribution of metal NPs in mTiO<sub>2</sub>. Thickness of spin-coated mTiO<sub>2</sub> film on FTO has been shown in Figure 4 (b), where a cross-sectional image has been taken by SEM. The thickness has been observed to be in the range of 4~5 microns. The synthesized Au-GSH NPs have been deposited on mTiO<sub>2</sub> photoanodes through immersion technique. The concentration of Au-GSH NPs in DI water was adjusted between 0.60~0.70 by wt. % in each case, and same immersion time for each photoanode

in Au-GSH NPs dispersions, indicates a uniform loading of metal NPs on the photoanodes.<sup>22</sup> The pH value should be between 2~6. In this pH range, the  $-\text{COO}^-$  group of glutathione molecule is electrostatically bonded with the positively charged  $\text{TiO}_2$ .<sup>32</sup> The pH value has been controlled within the above mentioned range to ensure fair comparison of each plasmonic sensitizer. The adjustment in pH was made through the addition of NaOH and acetic acid.

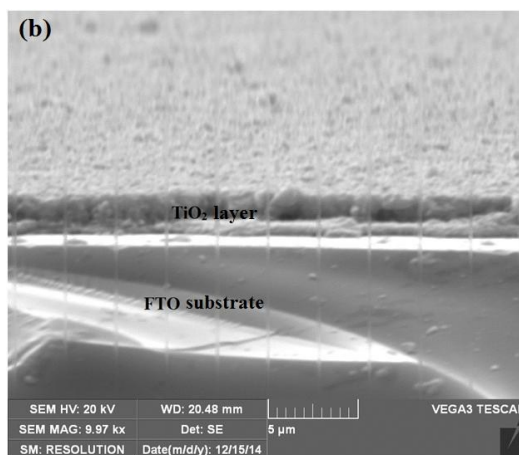
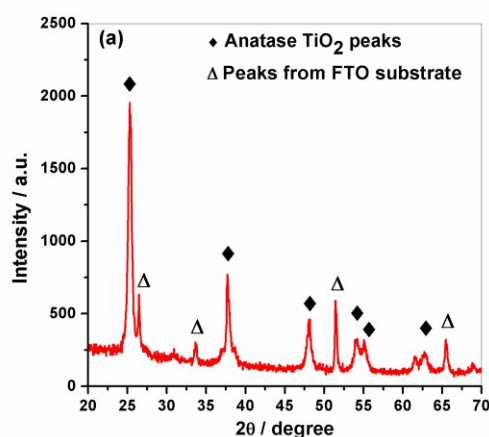


**Figure 4.** (a) XRD pattern of spin-coated  $\text{TiO}_2$  photoanode, and (b) SEM cross-sectional view of spin-coated  $\text{mTiO}_2$  film thickness on FTO substrate

SEM images of mTiO<sub>2</sub> photoanodes modified with Au-GSH-A, Au-GSH-B, Au-GSH-C and Au-GSH-D NPs are shown in Figure 5 (a-d), respectively. The EDX spectra of mTiO<sub>2</sub> modified with Au-GSH NPs are presented in the Figure S2 (e-h) along with corresponding SEM images (Figure S2 (a-d)). EDX spectra clearly indicate the presence of Au NPs on mTiO<sub>2</sub> semi-conductor. SEM morphology is apparently different in each mTiO<sub>2</sub> photoanode modified by different Au-GSH NPs, suggesting a variation in metal NPs distribution on TiO<sub>2</sub> photoanodes. It is expected that the variation in metal NPs distribution on TiO<sub>2</sub> photoanodes is due to deposition of different sized Au-GSH NPs with varied morphology, which may change the PEC performance of these plasmonic sensitizers.

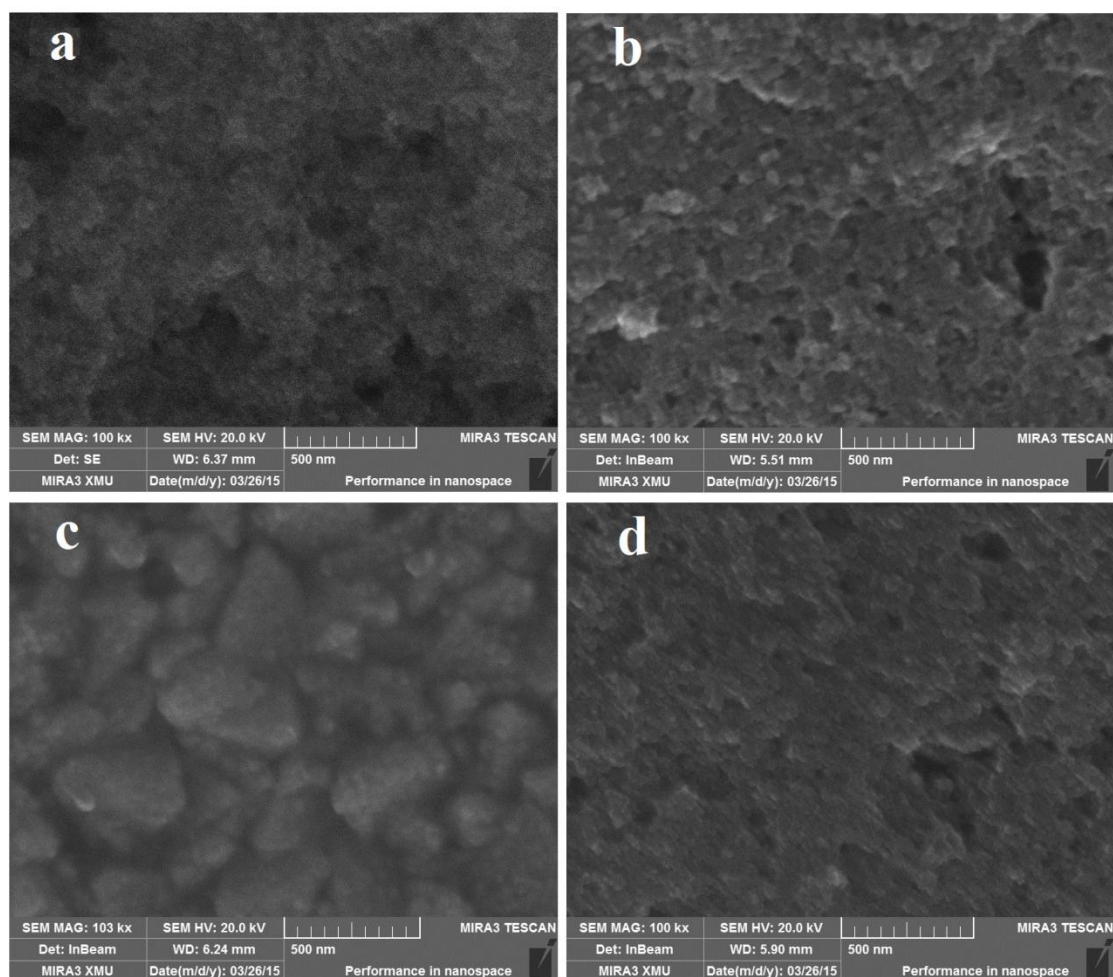


**Figure 5.** SEM images of (a) mTiO<sub>2</sub> modified with Au-GSH-A NPs, (b) mTiO<sub>2</sub> modified with Au-GSH-B NPs, (c) mTiO<sub>2</sub> modified with Au-GSH-C NPs, and (d) mTiO<sub>2</sub> modified with Au-GSH-D NPs.

### 3.4 Photo-electrochemical response of Au-GSH NPs as photo-sensitizers

PEC response depends on loading amount of sanitizers or dyes on metal oxide semiconductor coated on transparent conductive oxide (TCO). To ensure the same loading amount of Au NPs on TiO<sub>2</sub> photoanodes in each case, we have maintained the concentration of Au NPs in water between 0.60~0.70 wt. %. Equal immersion time was given to each TiO<sub>2</sub> photoanode so as to ensure same loading amount of sensitizer for a fair comparison, since the change in immersion time modifies the loading amount of sensitizer on photoanodes.<sup>22</sup> Active area of solar cells is same, therefore, it is expected that, given the same loading of sensitizers, the change in PEC response of NPSCs might be due to different sized Au-GSH NPs. PEC response of NPSCs fabricated from Au-GSH-A, Au-GSH-B, Au-GSH-C and Au-GSH-D NPs has been demonstrated in Figure 6. Figure 6a demonstrates J-V characteristics of Au-GSH NPs sensitizers under both dark and illumination conditions. Au-GSH-B NPs show the superior performance delivering short circuit current density ( $J_{sc}$ ) of 4.15 mA-cm<sup>-2</sup>,  $V_{oc}$  of 692 mV, FF of 45 % and PCE of 1.53%. Au-GSH-C CLs deliver  $J_{sc}$  of 4.08 mA-cm<sup>-2</sup>,  $V_{oc}$  of 615 mV, FF of 42 % and PCE of 1.26%. The higher values of  $J_{sc}$  in NPSCs constructed from Au-GSH-B and Au-GSH-C NPs are attributed to their higher light absorption. Relatively finer NPs size in Au-GSH-B NPs is likely one of the main factors that favor high  $J_{sc}$  on account of effective charge-carrier separation. Furthermore, smaller Au NPs shift the Fermi level more to the negative side than that of larger Au NPs, and improves the charge transfer efficiency.<sup>16</sup> It is expected that larger NPs (Au-GSH-D) might reduce the charge-carrier separation, and thus the PEC performance. Au-GSH-C NPs as sensitizers have a little higher dark current density in comparison with Au-GSH-B NPs which slightly degrades its performance and restricts the PCE

up to 1.26%. Dark current densities have also been shown in the Figure 6a. One can view that the dark current density is slightly larger in Au-GSH-C NPLs sensitizers (Figure 6a).

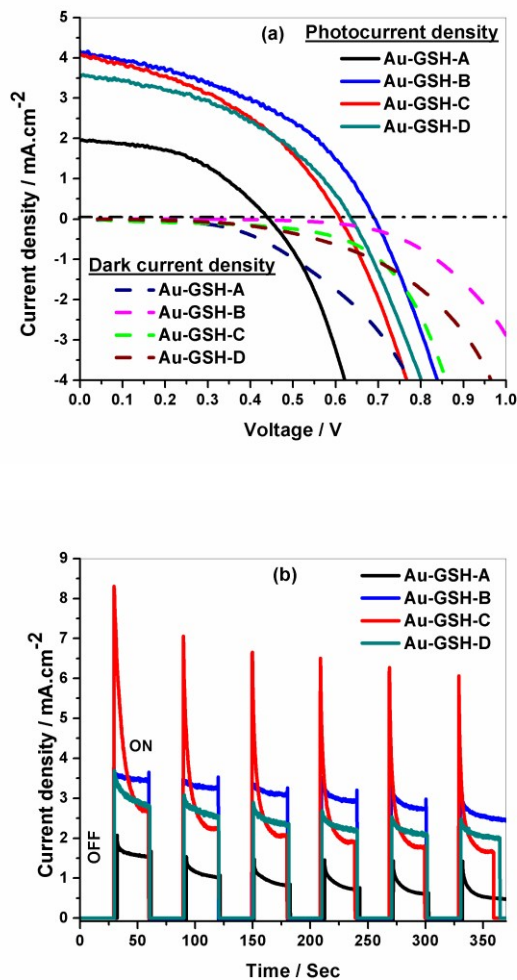


**Figure 6.** (a) J-V characteristics of NPSCs constructed from Au-GSH NPs as sensitizers, (b) Photocurrent stability of the NPSC fabricated from mTiO<sub>2</sub> modified with Au-GSH NPs under illumination on/off conditions.

Lower PEC performance of Au-GSH-A NPs sensitizers is expected due to their lower light absorption capability and incomplete formation of metal CLs and NPs at 25°C because their synthesis temperature is lower than what is required (70°C) for the formation of GSH-protected Au CLs.<sup>5, 26</sup> If Au-GSH-A NPs are synthesized at 70°C, the metal salt precursors in the presence

of ligands are reduced, and results in the formation of CLs, since some ligands can perform dual role: capping agent and reducing agent.<sup>19</sup> Au-GSH-D NPs have some agglomeration effect which might be responsible for lower PEC performance. Figure 6b manifests the behavior of  $J_{sc}$  with time for all NPSCs under investigation. When the illumination is off, the photocurrent in NPSCs approaches zero which again starts generating in the device when the illumination is on. The performance of NPSCs under illumination on/off cycle indicates the decay of  $J_{sc}$ . The decay of  $J_{sc}$  is less pronounced in Au-GSH-B NPs sensitizers. The results of photo-electrochemical measurements are summarized in Table-1.

**Table-1. PEC Characteristics of NPSCs**

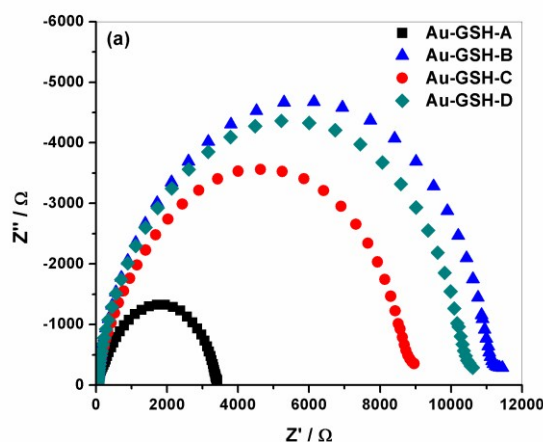
NPSCs	$J_{sc}$ (mA cm <sup>-2</sup> )	$V_{oc}$ (mV)	FF (%)	Efficiency (%)
Au-GSH-A	1.96	440	40	0.50
Au-GSH-B	4.15	692	45	1.53
Au-GSH-C	4.08	615	42	1.26
Au-GSH-D	3.52	636	44	1.22

The superior photovoltaic characteristics of glucose-assisted synthesis of Au-GSH-B NPs are assigned to relatively finer NPs morphology. The results presented in the Table-1 for NPSCs are relatively lower than those reported in the literature.<sup>5</sup> The potential reason for the lower performance, in our study, might be attributed to intrinsically different characteristics of Au NPs (in our study) and extremely small Au CLs reported in the literature.<sup>5</sup> Another possible reason is likely the lower loading amount of plasmonic sensitizers. Since, the main focus of the present study is to explore the imperative role of different sized Au NPs as plasmonic sensitizer on the

PEC performance, which has been realized through employing varied reductant and synthesizing a series of Au NPs with different sizes at ambient conditions.

### 3.5 Electron recombination kinetics and lifetimes

To investigate the processes occurring inside NPSCs, we perform electrochemical impedance spectroscopy. EIS is a steady-state method which has become a powerful tool to investigate the electrochemical and photo-electrochemical processes taking place in dye-sensitized solar cells. EIS generates Nyquist plots which normally represent two or three semicircles in the order of increasing frequency. These semi-circles are usually assigned to the Nernst diffusion within the electrolyte, the electron transfer at the semiconductor/electrolyte interface, and the redox reaction taking place at the counter electrode.<sup>33</sup> Electrochemical Impedance spectroscopy has been conducted under dark and graphically represented in Figure 7. Figures 7a and 7b show the Nyquist plots, whereas, Figure 7c shows the Bode phase plots under dark conditions. Figure 7b shows the Nyquist plots at an extended scale. The corresponding equivalent circuit has been shown in the Figure S3 which represents the processes taking place in a typical liquid DSSC.



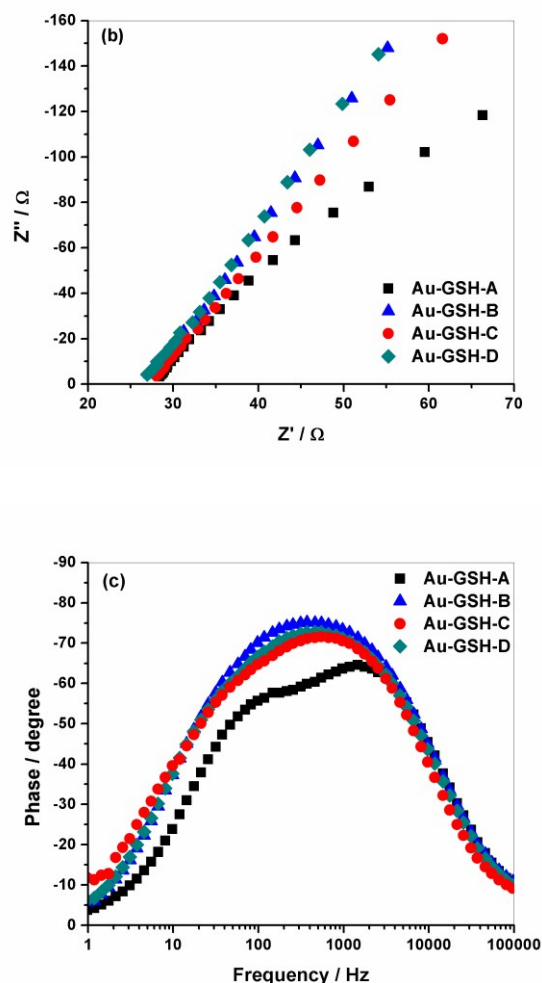


**Figure 7.** EIS spectra of NPSCs constructed from Au-GSH NPs as plasmonic sensitizers (a) Nyquist plots under dark conditions at 10mV amplitude, (b) Nyquist plots at an extended scale and (c) Bode phase plots showing the characteristic frequency

From the equivalent circuit,  $R_{pt}$ , in the high frequency region, indicates the resistance given by the sum of the CE/electrolyte and the FTO/TiO<sub>2</sub> interface.  $R_{rc}$  at medium frequency range is associated with the recombination interfacial resistance at TiO<sub>2</sub>/clusters/electrolyte interface. A small lowest frequency arc is generally attributed to the impedance of diffusion of redox species in the electrolyte i.e Warburg diffusion ( $W_s$ ). In our EIS experiment,  $R_{rc}$  is dominated  $W_s$  and  $R_{pt}$  because charge-transfer is the main process occurring at TiO<sub>2</sub>/NPs/electrolyte interface. Finally,

$R_s$  is the displacement of the arc which is attributed to the total series resistance of the solar cell.<sup>34</sup> We, herein, focus mainly on the middle frequency arc, since an identical Pt CE and same electrolyte have been used in the investigation. Therefore, it is expected that the change occurs only at  $\text{TiO}_2/\text{Au-GSH-NPs}/\text{electrolyte}$  interface. The smallest middle frequency arc diameter for NPSC constructed from Au-GSH-A NPs sensitizers indicates the lowest resistance at the  $\text{TiO}_2/\text{Au-GSH-NPs}/\text{electrolyte}$  interface, suggesting a higher recombination rate. NPSCs fabricated from  $\text{TiO}_2$  modified with Au-GSH-B NPs have higher value of FF which may be due to its lowest series resistance because  $R_s$  has direct influence on fill factor.<sup>35</sup> During synthesis of gold NPs, we used L-glutathione as a capping agent. We suppose that L-glutathione has same role in electron transfer kinetics and recombination dynamics, since ligand layer is expected to presence in each case.

Electron capturing by oxidizing species in the electrolyte is one of the main performance limiting phenomena. Due to a simple kinetic competition between charge collection and recombination; the power conversion efficiency of NPSC reduces when electron recombination rate accelerates and results in shorter electron lifetime. Moreover, we can make a comparison of the electron recombination lifetime or relaxation time constant from the Bode plots according to the relation:  $\tau_r = 1/\omega_{\max} = 1/2\pi f_{\max}$ , where,  $f_{\max}$  is the maximum frequency of the mid-frequency peak which has an inverse relation with electron lifetime i.e  $\tau_r$ <sup>36</sup>. The electron recombination lifetime is smaller for Au-GSH-A NPs consistent with the smallest arc diameter in the Nyquist plot. Furthermore, the peak frequency from the Bode phase diagrams is usually attributed to the recombination resistance.

<sup>33</sup> The characteristic peak frequency shifts towards higher frequency which shows the shorter electron lifetimes for Au-GSH-B NPs sensitizers (Figure 7c). EIS measurements show that Au-GSH-B NPs sensitizers demonstrate lower series resistance, lower recombination rate and longer electron lifetime, which collectively favor the superior performance of Au-GSH-B NPs.

Parameters evaluated from EIS spectra for each NPs type has been mentioned in Table-2. The calculated electron lifetimes are slightly larger than those reported in the literature for TiO<sub>2</sub> modified with Ag, largely due to different cell configuration and measuring conditions.<sup>37</sup>

**Table-2. Parameters Obtained through EIS Spectra and M-S Analysis**

NPSCs	R <sub>s</sub> (Ω)	Characteristic Frequency (Hz)	Electron Lifetime (ms)	Flat Band Potential (V)	N <sub>D</sub> (Conc. cm <sup>-3</sup> )
Au-GSH-A	28.35	1170	0.136	- 0.76	2.39883E+21
Au-GSH-B	26.95	371	0.428	- 0.89	2.13229E+22
Au-GSH-C	28.04	547	0.290	- 0.85	1.06615E+22
Au-GSH-D	27.10	459	0.346	- 0.78	7.46302E+21

To further investigate the electron recombination dynamics, we perform open-circuit voltage decay method. Figure 8 shows the transient open circuit voltage decay curves for all the NPs under investigation. In this method, at illumination, the solar cell has some V<sub>oc</sub>, which decays when illumination is switched off. Light source is suddenly turned off and allowed the test to continue at dark and monitored the decay of V<sub>oc</sub> with time. Decay of V<sub>oc</sub> is sluggish in Au-GSH-B NPs in comparison with Au-GSH-C and Au-GSH-D NPs. The sluggishness in Voc decay in Au-GSH-B NPs indicates the lower recombination rate kinetics. The steeper decay in Au-GSH-C NPs indicates the slightly higher recombination of photo-electrons.

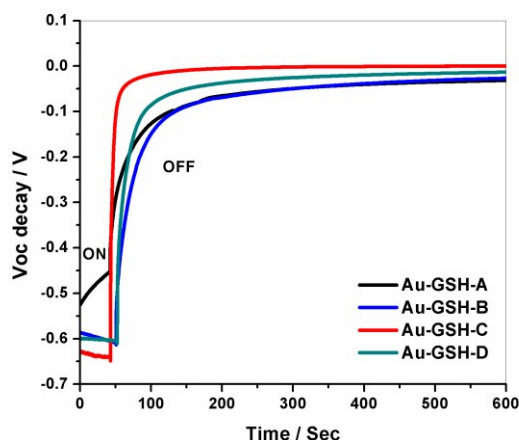


**Figure 8.** Transient open circuit voltage decay curves for NPSCs using mTiO<sub>2</sub> modified with Au-GSH NPs

### 3.6 Flat band potentials and carrier concentrations

The concentration of electrons in TiO<sub>2</sub> conduction band (CB) and the corresponding flat band potentials ( $E_{FB}$ ) are important parameters which need to be calculated at the junctions formed by Au metal and TiO<sub>2</sub> semiconductor. M-S analysis has been conducted to acquire the data for these parameters. Space charge capacitances are estimated from M-S plots so as to calculate donor density ( $N_D$ ) and  $E_{FB}$ , according to the following equation 1.<sup>38</sup>

$$C_{sc}^{-2} = 2/q\epsilon\epsilon_0 N_D A^2 (E - E_{FB} - KT/q) \quad (1)$$

where  $C_{sc}$  is the space charge capacitance ( $F\ cm^{-2}$ ),  $q$  is the electron charge ( $1.602E10^{-19}\ C$ ),  $\epsilon$  is the relative dielectric constant of the semiconductor (here we use  $\epsilon$  of anatase TiO<sub>2</sub> = 41.4)<sup>39</sup>,  $\epsilon_0$  is the permittivity of the vacuum ( $8.85E10^{-14}\ F\ cm^{-1}$ ),  $E$  is the applied potential (V),  $k$  is Boltzmann's constant ( $1.38E10^{-23}\ JK^{-1}$ ), and  $T$  is the absolute temperature (K). The slope of the linear region and the x-intercept of that linear region determine  $N_D$  and  $E_{FB}$  of the electrode, respectively.

Figure 9 shows the M-S plots for all sensitizers under study. One can observe the trend in slopes of linear regions of TiO<sub>2</sub> modified with different Au-GSH NPs. The obvious decline in the slope is an indicative of increasing carrier concentration.

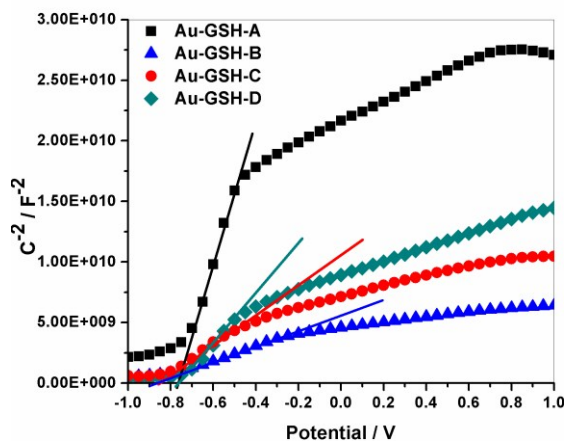


**Figure 9.** Mott-Schottky plots at 10mV amplitude for NPSCs fabricated by employing mTiO<sub>2</sub> modified with Au-GSH NPs plasmonic sensitizer.

The value of  $E_{FB}$  and  $N_D$  are mentioned in Table-2.  $E_{FB}$  becomes more negative for TiO<sub>2</sub> photoanodes modified with Au-GSH-B NPs. Highest  $J_{sc}$  obtained in Au-GSH-B NPs sensitized solar cells is likely due to its higher donor density, resulting from its higher light absorption and effective charge-carrier separation. It is expected that the shift in the Fermi level is more negative in Au-GSH-B NPs (finer NPs), with an attendant increase in carrier concentration in TiO<sub>2</sub> conduction band and improves the charge transfer efficiency.<sup>16</sup> The absorption is highest in Au-GSH-C NPs, but the relatively lower carrier concentration than that of Au-GSH-B NPs indicates a bit higher electron recombination rate. The lower carrier concentration due to electron recombination in Au-GSH-C NPs is consistent with its shorter electron lifetime and lower  $R_{rc}$ . The lower carrier concentration in Au-GSH-A and Au-GSH-D NPs is likely due to its lower optical absorption. The superior PEC performance manifested by Au-GSH-B NPs sensitizers may be due

to its lowest series resistance, highest optical absorption and highest donor density. Higher light absorption of Au-GSH-B NPs suggests its higher light harvesting efficiency (LHE), since the LHE is governed by the optical absorption, therefore, the higher  $J_{sc}$  in Au-GSH-B NPs sensitizers.<sup>40</sup>

The mechanism of charge movement in NPSC has been schematically demonstrated in Figure 10.

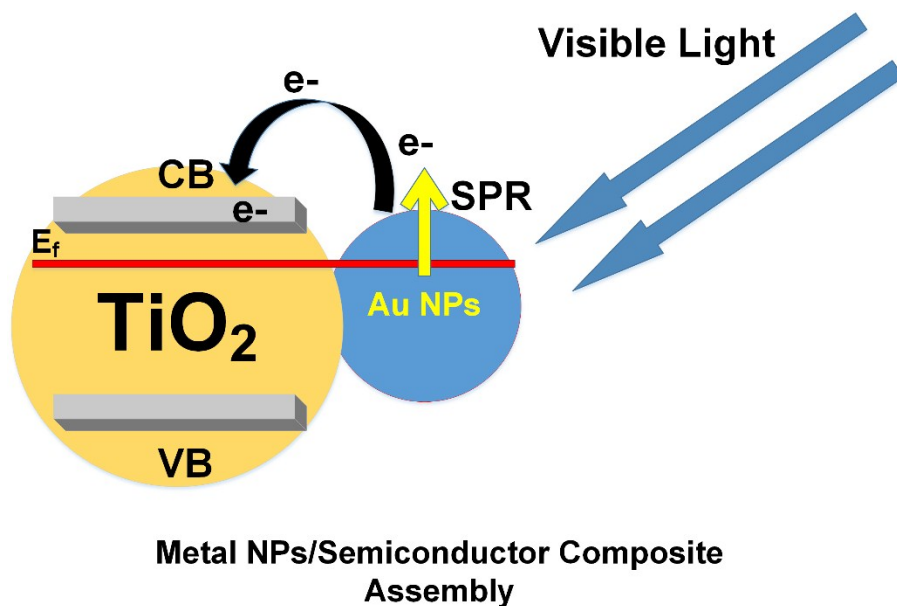


**Figure 10.** Schematic representation of the mechanism for the movement of charges in NPSCs with Au-GSH NPs as plasmonic sensitizer

It is well-known that Au NPs having diameters ranging from 1~10 nm would display electronic band structures owing to quantum mechanical rule.<sup>10</sup> It has also been reported that Au NPs with sizes in the range of 5-20 nm show a characteristic SPR phenomenon with the position of absorption peak varying with NPs morphology and NPs coating.<sup>28</sup> Virtually, Au NPs having these sizes should function as a sensitizer, since SPR behavior extends the light absorption capability through absorbing lower energy photons.

From the mechanism view points, the Fermi energy ( $E_f$ ) of Au is lower than that of  $TiO_2$ , therefore, the movement of electrons takes place from  $TiO_2$  to gold to equilibrate the Fermi levels. A

Schottky barrier is formed owing to Fermi energy alignment, thus, bending the valence band and conduction bands upward.<sup>41</sup> This transfer of electrons to gold causes the shift in Fermi-level in Au NPs/TiO<sub>2</sub> composite assembly to more negative potential, equilibrating the Fermi level with that of TiO<sub>2</sub>. This shift in Fermi level towards negative potentials causes the photo-generated charge transfer efficiency in Au NPs/TiO<sub>2</sub> composite assembly.<sup>17</sup> As shown schematically in Figure 10, upon visible-light irradiation, SPR-excitation generates photoelectrons which are injected into TiO<sub>2</sub> CB overcoming the energy barrier.<sup>11</sup> Apart from SPR-excitation, the local electromagnetic field enhancement through SPR phenomenon is another important phenomenon which reinforces the charge carrier generation by effectively separating them.<sup>42</sup> The injected electrons are transported through TiO<sub>2</sub> CB to the current collector and reduce redox-couple at the counter electrode (CE). CE and redox-couple in the electrolyte are at the same potentials, and voltage between the donors in the electrolyte and the TiO<sub>2</sub> CB is a constant, therefore, the  $V_{oc}$  of the working electrode is possibly determined by the number of photoelectrons injected from Au NPs to TiO<sub>2</sub> CB. The higher the quantity of injected photoelectrons, the larger would be the resultant  $V_{oc}$  in the system. The higher  $N_D$  value observed in Au-GSH-B NPs sensitizers results in higher  $V_{oc}$  consistent with the J-V characteristics. Higher  $N_D$  value shifts the quasi-Fermi level upward, which results in larger open circuit voltage. The current generation in the actual working conditions of metal cluster-sensitized solar cells, the cell's generated constant current is equal to the sum of photo-generated current and dark current minus the current owing to back reactions and leakage or shunting. The PEC performance of all sensitizers under investigation is not very high, since the loading of sensitizer on TiO<sub>2</sub> is not high enough owing to the low concentration of metal NPs (0.60~0.70 wt% in DI water), and the absence of TiO<sub>2</sub> blocking layer on FTO. The TiO<sub>2</sub> blocking layer is beneficial to reduce the electron recombination as reported by elsewhere.<sup>43</sup>

In summary, the Au-GSH-B NPs synthesized using glucose as a reductant are more efficient in comparison with Au-GSH-A, Au-GSH-C and Au-GSH-D NPs; predominately, owing to the higher optical absorption, lowest series resistance and highest donor density. The superior PEC response indicates that glucose in coordination with glutathione ligand assists in the formation of finer NPs and their uniform distribution with minimal aggregation, which ultimately result in higher PEC performance. Our experimental study reveals that PEC performance of plasmonic sensitizer varies with their NPs sizes, and the efforts are under way to couple these different sized Au NPs with some suitable dyes to optimize the photovoltaic characteristics in dye-sensitized solar cells.

#### **4. Conclusions**

We have successfully synthesized and characterized Au-GSH NPs having varied sizes using different reductants at ambient conditions, followed by manifestation of their functional performance as plasmonic sensitizer in NPs-sensitized solar cells. The reaction dynamics and resultant NPs morphology are influenced by the interaction of reductant with ligand. Superior PEC response was observed in glucose-assisted synthesis of Au-GSH NPs, and attributed to the relatively finer NPs sizes and uniform distribution on TiO<sub>2</sub> photoanodes, resulting in an improved power conversion efficiency greater than 1.5 %. The higher optical absorption, lowest series resistance, sluggish electron recombination kinetics and highest carrier concentration have further corroborated the imperative role of finer Au-GSH NPs towards improving the PEC performance. We expect that our study contribute significantly to synthesis chemistry and assists in exploration of different sized metal NPs in a diverse range of energy and medical applications.

## Acknowledgments

This study has been supported by the National Natural Science Foundation of China (grant nos. 51271148 and 50971100), the Research Fund of State Key Laboratory of Solidification Processing in China (grant no. 30-TP-2009), and the Aeronautic Science Foundation Program of China (grant no. 2012ZF53073), and the Doctoral Fund of Ministry of Education of China (grant no. 20136102110013)

## Notes

The authors declare no competing financial interests

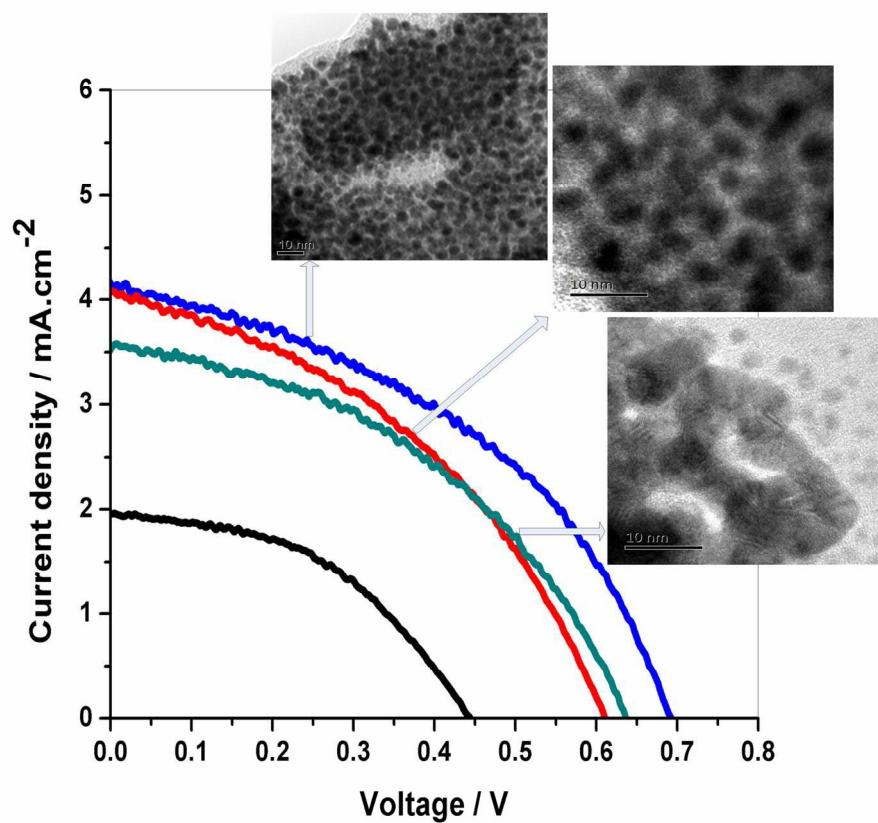
## References

1. B. Oregan and M. Gratzel, *Nature*, 1991, 353, 737-740.
2. M. Gratzel, *J Photoch Photobio C*, 2003, 4, 145-153.
3. W. Zhang, M. Saliba, S. D. Stranks, Y. Sun, X. Shi, U. Wiesner and H. J. Snaith, *Nano Lett*, 2013, 13, 4505-4510.
4. M. Zhu, C. M. Aikens, F. J. Hollander, G. C. Schatz and R. Jin, *J Am Chem Soc*, 2008, 130, 5883-5885.
5. Y. S. Chen, H. Choi and P. V. Kamat, *J Am Chem Soc*, 2013, 135, 8822-8825.
6. A. Kogo, N. Sakai and T. Tatsuma, *Nanoscale*, 2012, 4, 4217-4221.
7. E. B. Guidez, V. Mäkinen, H. Hakkinen and C. M. Aikens, *J Phys Chem C*, 2012, 116, 20617-20624.
8. N. Sakai, S. Nakamura and T. Tatsuma, *Dalton T*, 2013, 42, 16162-16165.
9. N. Shahzad, F. Chen, L. He, W. Li and H. Wang, *J Power Sources*, 2015, 294, 609-619.
10. M. C. Daniel and D. Astruc, *Chem Rev*, 2004, 104, 293-346.

11. Y. Tian and T. Tatsuma, *J Am Chem Soc*, 2005, 127, 7632-7637.
12. S. J. Oldenburg, S. L. Westcott, R. D. Averitt and N. J. Halas, *J Chem Phys*, 1999, 111, 4729-4735.
13. X. C. Pang, L. Zhao, W. Han, X. K. Xin and Z. Q. Lin, *Nat Nanotechnol*, 2013, 8, 426-431.
14. H. J. Kim, S. H. Lee, A. A. Upadhye, I. Ro, M. I. Tejedor-Tejedor, M. A. Anderson, W. B. Kim and G. W. Huber, *Acs Nano*, 2014, 8, 10756-10765.
15. X. O. Liu, M. Atwater, J. H. Wang and Q. Huo, *Colloid Surface B*, 2007, 58, 3-7.
16. V. Subramanian, E. E. Wolf and P. V. Kamat, *J Am Chem Soc*, 2004, 126, 4943-4950.
17. M. Jakob, H. Levanon and P. V. Kamat, *Nano Lett*, 2003, 3, 353-358.
18. X. H. Ji, X. N. Song, J. Li, Y. B. Bai, W. S. Yang and X. G. Peng, *J Am Chem Soc*, 2007, 129, 13939-13948.
19. N. Ortiz and S. E. Skrabalak, *Langmuir*, 2014, 30, 6649-6659.
20. M. Mohl, P. Pusztai, A. Kukovecz, Z. Konya, J. Kukkola, K. Kordas, R. Vajtai and P. M. Ajayan, *Langmuir*, 2010, 26, 16496-16502.
21. Z. H. Chen, Y. B. Tang, C. P. Liu, Y. H. Leung, G. D. Yuan, L. M. Chen, Y. Q. Wang, I. Bello, J. A. Zapien, W. J. Zhang, C. S. Lee and S. T. Lee, *J Phys Chem C*, 2009, 113, 13433-13437.
22. F.X. Xiao, Z. Zeng and B.Liu, *J Am Chem Soc*, 2015, DOI: 10.1021/jacs.5b06323.
23. K. G. Stampeleskie and P. V. Kamat, *J Phys Chem Lett*, 2015, 6, 1870-1875.
24. W. Jiang, B. Y. S. Kim, J. T. Rutka and W. C. W. Chan, *Nat Nanotechnol*, 2008, 3, 145-150.
25. J. H. Wu, G. T. Yue, Y. M. Xiao, J. M. Lin, M. L. Huang, Z. Lan, Q. W. Tang, Y. F. Huang, L. Q. Fan, S. Yin and T. Sato, *Sci Rep-Uk*, 2013, 3.

26. Z. T. Luo, X. Yuan, Y. Yu, Q. B. Zhang, D. T. Leong, J. Y. Lee and J. P. Xie, *J Am Chem Soc*, 2012, 134, 16662-16670.
27. T. Udayabhaskararao, M. S. Bootharaju and T. Pradeep, *Nanoscale*, 2013, 5, 9404-9411.
28. H. Yu, M. Chen, P. M. Rice, S. X. Wang, R. L. White and S. H. Sun, *Nano Lett*, 2005, 5, 379-382.
29. H. Y. Yang, Y. Wang, H. Q. Huang, L. Gell, L. Lehtovaara, S. Malola, H. Hakkinen and N. F. Zheng, *Nature Communications*, 2013, 4.
30. W. Shao, F. Gu, C. Z. Li and M. K. Lu, *Ind Eng Chem Res*, 2010, 49, 9111-9116.
31. Q. H. Zhang, L. Gao and J. K. Guo, *Appl Catal B-Environ*, 2000, 26, 207-215.
32. N. Sakai and T. Tatsuma, *Adv Mater*, 2010, 22, 3185-+.
33. X. Zhang, F. Liu, Q. L. Huang, G. Zhou and Z. S. Wang, *J Phys Chem C*, 2011, 115, 12665-12671.
34. C. Longo, A. F. Nogueira, M. A. De Paoli and H. Cachet, *J Phys Chem B*, 2002, 106, 5925-5930.
35. B. L. He, X. Meng and Q. W. Tang, *Acs Appl Mater Inter*, 2014, 6, 4812-4818.
36. S. Lee, J. H. Noh, H. S. Han, D. K. Yim, D. H. Kim, J. K. Lee, J. Y. Kim, H. S. Jung and K. S. Hong, *J Phys Chem C*, 2009, 113, 6878-6882.
37. S. P. Lim, A. Pandikumar, N. M. Huang and H. N. Lim, *Rsc Adv*, 2014, 4, 38111-38118.
38. D. a. M.-S. Hyoungh-il Kim, Wooyul Kim and Wonyong Choi, *Energy Environ. Sci*, 2015, 8, 247-257.
39. J. Y. Kim, H. S. Jung, J. H. No, J. R. Kim and K. S. Hong, *J Electroceram*, 2006, 16, 447-451.
40. K. Miettunen, J. Halme, A. M. Visuri and P. Lund, *J Phys Chem C*, 2011, 115, 7019-7031.

41. A. Stevanovic, S. L. Ma and J. T. Yates, *J Phys Chem C*, 2014, 118, 21275-21280.
42. Z. W. Liu, W. B. Hou, P. Pavaskar, M. Aykol and S. B. Cronin, *Nano Lett*, 2011, 11, 1111-1116.
43. K. Miettunen, J. Halme, P. Vahermaa, T. Saukkonen, M. Toivola and P. Lund, *J Electrochem Soc*, 2009, 156, B876-B883.



Influence of nano-particles sizes on photovoltaic characteristics  
76x67mm (600 x 600 DPI)